

Tide-Surge Interaction observed at Singapore and the east coast of Peninsular Malaysia using a Semi-empirical Model

Zhi Yang Koh¹, Benjamin S. Grandey¹, Dhrubajyoti Samanta², Adam D. Switzer^{2,3}, Benjamin P. Horton^{2,3}, Justin Dauwels⁴, Lock Yue Chew¹

¹School of Physical and Mathematical Sciences, Nanyang Technological University, Singapore

²Earth Observatory of Singapore, Nanyang Technological University, Singapore

³Asian School of the Environment, Nanyang Technological University, Singapore

⁴Department of Microelectronics, Faculty of Electrical Engineering, Mathematics, and Computer Science, Delft University of Technology (TU Delft), The Netherlands

Correspondence to: Zhi Yang Koh (kohz0034@e.ntu.edu.sg)

Abstract. Tide-surge interaction plays a substantial role in determining the characteristics of coastal water levels over shallow regions. We study the tide-surge interaction observed at seven tide gauges along Singapore and the east coast of Peninsular Malaysia, focusing on the timing of extreme non-tidal residuals relative to tidal high water. We propose a modified statistical framework using a No-Tide-Surge Interaction (No-TSI) null distribution that accounts for asymmetry and variation in the duration of tidal cycles. We find that our modified framework can mitigate false positive signals of tide-surge interaction in this region. We find evidence of tide-surge interaction at all seven locations, with characteristics varying smoothly along the coastline: the highest non-tidal residuals are found to occur most frequently before tidal high water at the south, both before and after tidal high water at the middle, and after tidal high water at the north. We also propose a semi-empirical model to investigate the effects of tidal phase alteration, which is one mechanism of tide-surge interaction. Results of our semi-empirical model reveal that tidal phase alteration caused by storm surges is substantial enough to generate significant change in the timing of extreme non-tidal residuals. To mitigate the effect of tidal phase alteration on return level estimation, skew surge can be used. We conclude that (1) tide-surge interaction influences coastal water levels in this region, (2) our semi-empirical model provides insight into the mechanism of tidal phase alteration, and (3) our No-TSI distribution should be used for similar studies globally.

27 **Short summary**

28 Identifying tide-surge interaction (TSI) is a complex task. We enhance existing statistical methods with a
29 more robust test that accounts for complex tides. We also develop a semi-empirical model to investigate
30 the influence of one mechanism of TSI, tidal phase alteration. We apply these techniques to tide-gauge
31 records from Singapore and the east coast of Peninsular Malaysia. We find TSI at all studied locations:
32 tidal phase alteration can change the timing of large surges.

33 **1 Introduction**

34 Coastal regions are vulnerable to the combined effects of tides and storm surges, which can induce
35 significant sea-level variations and pose substantial risks to coastal communities and ecosystems (Diaz,
36 2016; von Storch et al., 2015; Hinkel et al., 2014). Storm surges are rises in sea level brought about by
37 low atmospheric pressure and strong winds acting on the sea surface (Pugh and Woodworth, 2014a).
38 Large storm tides occur when large storm surges coincide with high tides (Stephens et al., 2020; Gregory
39 et al., 2019), which increase the risk of coastal flooding and threaten lives and livelihoods (Pugh and
40 Woodworth, 2014c). The likelihood and impact of such destructive events are further aggravated by sea-
41 level rise (Calafat et al., 2022; Marcos and Woodworth, 2017; Woodworth and Blackman, 2004). To
42 identify the appropriate response to such extreme water level events, we must understand the fundamental
43 processes of tides and storm surges and their mutual interactions.

44 A dependence between tides and surges has long been noticed at coastal locations (Keers, 1968),
45 and recognised to be caused by interaction between tides and surges (Pugh and Vassie, 1978; Wolf, 1978).
46 Understanding tidal dynamics, surge generation, and their mutual interaction is required to improve
47 operational forecasts of sea levels and the statistical estimation of its extremes (Olbert et al., 2013;
48 Horsburgh and Wilson, 2007; Tawn and Vassie, 1989). This tide-surge interaction is non-linear and can
49 lead to complex coastal dynamics characterized by amplification or attenuation of water levels, which are
50 influenced by local bathymetry, coastline geometry, and atmospheric conditions (Idier et al., 2019).
51 Strong tide-surge interaction has been observed in shallow waters and estuaries (Wolf, 1981) and hence
52 is expected at the Sunda Shelf where Singapore and Malaysia are located. The main mechanism behind

53 tide-surge interaction is mutual phase alteration (Rossiter, 1961). The generation of surges over a water
54 body is influenced by the depth of the water body. As changes in depth occur partially due to tides, the
55 height of surges can be influenced by tides. The propagation speed of tides is also dependent on depth,
56 which can change due to surges (Proudman, 1957, 1955). Further studies that analysed shallow-water
57 equations along the coast found that the non-linear tide-surge interaction is caused by the advection term,
58 non-linear bottom friction term, and the non-linear shallow water effects of the shallow-water equations
59 (Zhang et al., 2021; Idier et al., 2012).

60 Studies of tide-surge interaction have employed a range of modelling approaches, including
61 statistical methods (Arns et al., 2020; Haigh et al., 2010; Dixon and Tawn, 1994), numerical models
62 (Costa et al., 2023; Horsburgh and Wilson, 2007; Prandle and Wolf, 1978), and analytical models
63 (Horsburgh and Wilson, 2007). Dixon and Tawn (1994) proposed a statistical framework where they split
64 the tidal range into five equiprobable bands and used a chi-square test to determine whether non-tidal
65 residuals above a height threshold fall uniformly into each band. Horsburgh and Wilson (2007) proposed
66 a modified version of the framework where the tide is instead split into 13 hourly bands between 6.5 hours
67 before and after tidal high water (HW). Horsburgh and Wilson (2007) also provided a simple
68 mathematical explanation for the abundance of large non-tidal residuals at timings halfway between tidal
69 low water and HW.

70 Application of such frameworks revealed that extreme residuals are most often found 3–5 hours
71 before HW in the Bay of Bengal (Antony and Unnikrishnan, 2013) and the North Sea (Horsburgh and
72 Wilson, 2007), and typically about 2 hours before HW in the English Channel (Haigh et al., 2010). In
73 China and New Zealand, observed tide-surge interaction varies along the coastline: the frequency of
74 extreme residuals peaks before HW at certain locations, after HW at others, and is independent of tides
75 at the remaining locations (Costa et al., 2023; Feng et al., 2019). Numerical models have shown that the
76 inclusion of tide-surge interaction often results in better water level predictions, especially over coastal
77 and shelf waters, whereas the omission of the interaction may lead to under or overestimation of surges
78 at certain locations (Fernández-Montblanc et al., 2019; Idier et al., 2012). For example, Antony et al.
79 (2020) showed that numerically modelled peak water levels generated during Cyclone Aila at the head of
80 the Bay of Bengal would have been overestimated if tide-surge interaction was not simulated.

81 Here, we focus on investigating tide-surge interaction observed at seven tide gauge locations near
82 Singapore and the east coast of Peninsular Malaysia using modified statistical methods and a new semi-
83 empirical model. Our research objectives are (1) examining the tide gauge records to characterise the tide-
84 surge interaction observed at each tide gauge location and the spatial pattern across locations, and (2)
85 explaining the observed interaction characteristics through a simple semi-empirical model.

86 We apply a modified version of the statistical method by Horsburgh and Wilson (2007) to
87 determine the presence of tide-surge interaction at each tide gauge location and to characterise these
88 interactions. The existing method groups residuals above a height threshold into 13 hourly bands between
89 6.5 hours before and after HW, counts the number of residuals in each band and compares the resulting
90 distribution to the uniform distribution using a chi-square test. However, due to asymmetry and variation
91 in the duration of tidal cycles (Guo et al., 2019), the expected null distribution would not be a uniform
92 distribution over 13 hourly bands centred at HW especially at locations with mixed or diurnal tides lasting
93 up to 25 hours. Hence, our key modification to the existing methodology is to replace the uniform
94 distribution with a “No-TSI distribution” as the null distribution. We also use an exact statistical test for
95 hypothesis testing instead of the chi-square test. In addition, we propose a simple approach to compare
96 the tide-surge interaction across locations that have different tidal characteristics (diurnal, mixed, or
97 semidiurnal).

98 We aim to provide an explicit explanation of the observed tide-surge interaction through our semi-
99 empirical model by combining historical tide and surge data with winds, coastal geometry, and
100 bathymetry. The semi-empirical model accounts for the mechanism of tidal phase alteration: storm surges
101 perturb the depth of the water body which influences the propagation speed of the tide. This results in
102 differences between observed tides and tides predicted from harmonic analysis, which are detected as
103 non-tidal residuals. We use our model to show that this mechanism can significantly influence the timing
104 of extreme residuals to produce signals of tide-surge interaction.

105 **2 Singapore and the east coast of Peninsular Malaysia**

106 The seven tide gauges are located within the Sunda Shelf, illustrated in Fig. 1a, which has a typical depth
107 of 40–80 m. The shallowness of this shelf likely enhances the interaction between tide and surge, and its

108 expanse allows for phase changes in the tides to compound as the tide propagates across the shelf. The
109 eastern coastline of Peninsular Malaysia faces the South China Sea and is exposed to strong seasonal
110 monsoon winds resulting in larger surges (Mohd Anuar et al., 2020). To the north of our study region lies
111 the Gulf of Thailand. To the south of Singapore, the southernmost location of our study region, lies part
112 of the Riau Islands, Sumatra, the Karimata Strait and the Java Sea. The Malacca Strait is west of Singapore
113 and leads to the Indian Ocean. The diurnal and semidiurnal tides that propagate from the South China Sea
114 and the Indian Ocean respectively drive the complex mixed tides in Singapore and the Southern parts of
115 the study region (van Maren and Gerritsen, 2012). At Singapore, the diurnal tides that propagate from the
116 South China Sea get further amplified from reflection against the east coast of Sumatra (van Maren and
117 Gerritsen, 2012).

118 A close-up of the bathymetry around the seven stations is shown in Fig. S1 and detailed maps of
119 their immediate vicinity are shown in Fig. 1b–h and S2. Of our seven tide gauges, Tanjong Pagar and
120 Johor Baharu are located within straits, Sedili at a river mouth, Tioman between Tioman island and
121 mainland Peninsular Malaysia sheltered from the South China Sea, Kuantan at the mouth of a man-made
122 bay, Cendering on the open coast and Geting sheltered inside a bay.

123 Monsoonal winds are the main determining factor of hourly surges and their extremes in the
124 Singapore Strait (Tkalic et al., 2013a, 2009). Storm surges occur along the coast throughout the year,
125 reaching 0.35–1.0 m at Geting, the northernmost location of our study region (Abd Razak et al., 2024).
126 The northern part of the coast is more prone to stronger storm surges due to tropical depressions (Mohd
127 Anuar et al., 2023). In the southern part of the coast, a surge of about 1.0 m caused by Typhoon Vamei in
128 2001 was recorded (Mohd Anuar et al., 2018). Several storm surge events in Singapore reaching 0.3–0.8
129 m have also been documented since 1974 (Luu et al., 2016), particularly during the winter monsoon
130 period.

131 Our analysis found that the tidal range in this region can reach 2.7–3.6 m and the largest non-tidal
132 residuals over the past 30 years exceed 0.8 m. Understanding how these components interact and combine
133 provides insight into the contributors to coastal water levels. Hydrodynamical processes, mainly those
134 caused by regional wind forcing during the seasonal monsoons, have shown a strong influence on the

135 water levels at the seven tide gauges analysed in this study (Tay et al., 2016; Luu et al., 2016; Kurniawan
136 et al., 2015; Karri et al., 2014; Tkalich et al., 2013a; Chen et al., 2012).

137 **3 Data and methods**

138 The general methodology begins with separating hourly tide gauge data into tides and non-tidal residuals.
139 Following the methodology of Horsburgh and Wilson (2007), we identify the largest non-tidal residuals
140 and find their timings relative to their nearest tidal high water and tabulate it as a frequency distribution.
141 Next, we calculate the No-TSI distribution. We compare the frequency distribution to the No-TSI
142 distribution using hypothesis testing to determine the presence of tide-surge interaction. We then generate
143 model residuals using our semi-empirical model and repeat the above procedure to determine if tide-surge
144 interactions are generated by our model. We use research quality hourly tide gauge data obtained from
145 the University of Hawaii Sea Level Center. Bathymetry, hourly 10 m winds and mean sea level pressure
146 are obtained from ERA5.

147 **3.1 Tide gauge data, tides and residuals**

148 Research quality hourly water level from tide gauges at seven locations (Fig. 1) along Singapore and the
149 east coast of Peninsular Malaysia are obtained from the University of Hawaii Sea Level Center (Caldwell
150 et al., 2001). Details of the tide gauge records are tabulated in Table 1. Observations have been made over
151 at least 29 years at each location with a data completion rate of 95–99 %. The length of these records is
152 close to the 30-year threshold typically considered the minimum length required for analysis of extreme
153 sea levels (Rasmussen et al., 2018). Nonetheless, these stations have some of the longest records within
154 Southeast Asia (Caldwell et al., 2001).

155 To compute the tidal level and non-tidal residuals, we use the equation
156

$$157 \quad X(t) = Z(t) + T(t) + R(t). \quad (1)$$

158

159 $X(t)$ is the hourly water level recorded by a tide gauge at time t . $Z(t)$ is the 1-year (8766-hour after
160 accounting for leap years) moving average of $X(t)$. A 1-year window was chosen because intra-annual

behaviour of residuals is well understood to be periodic due to seasonal variations, and its influence on residuals is of interest in this study (Tkalic et al., 2013b). Detrending the hourly water level by the 1-year moving average removes trends of annual and longer timescales from the tide gauge records. The 1-year moving average is calculated only if at least 85 % of the data in the 8766-hour window is available. This reduces our usable data to 87–99 % across the seven locations. The standard deviation and certain key quantiles of the detrended water level, $X(t) - Z(t)$, are tabulated in Table 2. While water levels of this height do not pose an immediate threat to the region, understanding the underlying drivers is integral for applications such as early detection of extreme events, forecasting, or coastal protection design purposes especially with sea level rise and the increasing frequency and intensity of storms (Mohd Anuar et al., 2018). $T(t)$ is the tidal level which we estimate using UTide, a tidal harmonic analysis package implemented in Matlab (Codiga, 2011). $X(t) - Z(t)$ is split into two halves based on the start and end dates in Table 1 and used as inputs to UTide, as UTide does not recommend using records longer than 18.6 years as input. UTide was used to identify the amplitudes and phases of 66 tidal constituents with periods of up to 32 days through harmonic analysis. Constituents with a signal-to-noise ratio of at least 2 are used to construct $T(t)$. $R(t)$, the residual, is then estimated as $R(t) = X(t) - Z(t) - T(t)$. We denote the residual obtained through this procedure as R_{gauge} . The time-series of $X(t) - Z(t)$, $T(t)$ and R_{gauge} at each tide gauge during their largest recorded R_{gauge} are illustrated in Fig. S3.

A summary of the tidal characteristics at the seven locations is tabulated in Table 3. The tides at these locations lie within the microtidal (<2 m) and mesotidal (2–4 m) ranges with diurnal tidal ranges of close to 2 m except at Cendering and Geting where diurnal tidal ranges are 1.5 m and 0.8 m respectively. We found that the daily tidal range can be as large as 3.6 m at Johor Baharu and Kuantan, similar to other studies (Ismail et al., 2018; Ng and Sivasothi). In a shelf with a depth of 40–80 m, tides of 3.6 m produce a water depth deviation from its mean by up to about ± 4 %. The tides at a location can be categorised into diurnal, semi-diurnal, or mixed using the tidal form factor F which compares the relative importance of the following diurnal and semidiurnal tidal constituents (Pugh and Woodworth, 2014b):

$$F = \frac{K_1 + O_1}{M_2 + S_2}. \quad (2)$$

189 A common classification considers a location with a factor of <0.25 to be semidiurnal, $0.25\text{--}1.50$ to be
 190 mixed with mainly semidiurnal tides, $1.50\text{--}3.00$ to be mixed with mainly diurnal tides and >3.00 to be
 191 diurnal (Pugh and Woodworth, 2014b). Based on this classification, the tides at all stations are identified
 192 to be mixed, with Cendering and Geting being mainly diurnal while all other stations to the south are
 193 mainly semidiurnal. Out of all tidal constituents estimated across seven locations, we find that the
 194 amplitude of most constituents does not change by more than 5 mm between the first and second half of
 195 their tide gauge records while eight constituents saw a change of 5–13 mm. The change in mean diurnal
 196 tidal range is about 0.2 cm at Tanjong Pagar to 4.9 cm at Geting. Attribution of these changes remains a
 197 difficult task and is outside the scope of this study, but some local drivers include (1) dissipation and
 198 turbulent mixing; (2) depth of channels and flats; (3) surface area, width, and convergence; (4) resonance
 199 and reflection; (5) river flow; and (6) changes in instrumentation (Haigh et al., 2020).

200 **3.2 Identifying tide-surge interaction**

201 To determine whether tide-surge interaction is present at each of the seven tide gauge locations, we apply
 202 a modified version of the statistical method by Horsburgh and Wilson (2007) on the processed tide gauge
 203 records (Sect. 3.1). This method compares the timing of extreme residuals to the nearest HW.

204 To identify extreme residuals, the 99th percentile and above of R_{gauge} are identified. There are
 205 many clusters of R_{gauge} above this threshold, where a cluster refers to a collection of R_{gauge}
 206 consecutively measured, each measured 1 hour from the last. The largest R_{gauge} in each cluster is
 207 identified and sorted. Starting from the largest, the sorted R_{gauge} are added to the set of extreme R_{gauge}
 208 unless the R_{gauge} was measured within 1 week (168 hours) of another extreme R_{gauge} in the set. Some
 209 other thresholds used in published studies range from 12–60 hours (Arns et al., 2020; Feng et al., 2019;
 210 Rasmussen et al., 2018; Buchanan et al., 2016; Horsburgh and Wilson, 2007). We choose a threshold of
 211 1 week to reduce the odds of double counting long-lasting surges, as such events can last between 1 and
 212 5 days in this region (Meteorological Service Singapore; Cannaby et al., 2016; Marzin et al., 2015;
 213 Tkalic et al., 2009). We also found statistically significant autocorrelation in the R_{gauge} time-series at

time lags shorter than 168 hours. A declustering threshold of 168 hours still retain sufficient observations for our analysis.

To compare locations with predominantly semidiurnal tides with locations with predominantly diurnal tides, we split the extreme R_{gauge} into two groups. We define a tidal cycle as the duration from one local minima in $T(t)$ to the observation immediately preceding the next local minima as illustrated in Fig. 2b. One group of extreme R_{gauge} were observed during tidal cycles of 21 hours or shorter, representing extreme residuals that occurred during semidiurnal cycles. The other group contain extreme R_{gauge} observed during tidal cycles of at least 22 hours, representing extreme residuals that had occurred during diurnal tides. This separation between 21-hours-or-less and 22-hours-or-more was chosen based on the characteristics of the duration of tidal cycles at the seven locations, where the distribution of the duration of tidal cycles was found to be bimodal at each location and the 22-hour mark tends to distinguish the two modes (Fig. S4).

The HW in the same tidal cycle as each extreme R_{gauge} is identified and the timing difference between the extreme R_{gauge} and the respective HW is quantified at hourly resolution. Across the set of extreme R_{gauge} , the frequency of extreme R_{gauge} found a certain number of hours relative to HW, h , is counted. This frequency is plotted as a *frequency distribution* in the form of a histogram (Fig. 3). The magnitude of each extreme R_{gauge} is represented by colour in the frequency distribution. Box plots below the histograms show the median and its 95 % confidence interval, the interquartile range (IQR), a range that extends up to $1.5 \times \text{IQR}$ from the limits of the IQR, and the outliers (Fig. 3).

We use the frequency distribution to test the null hypothesis that assumes that there is no tide-surge interaction. To do so, we test whether the frequency distribution is drawn from a null distribution representing a scenario where extreme events are equally likely to occur at any stage of a tidal cycle.

3.3 No-Tide-Surge Interaction distribution

In existing studies, the null distribution is a uniform distribution with a value of $n/13$ at $h = -6, -5, \dots, 0, \dots, 5, 6$ where n is the total number of extreme events (Horsburgh and Wilson, 2007; Haigh et al., 2010; Antony and Unnikrishnan, 2013; Feng et al., 2019; Costa et al., 2023). It assumes that tidal cycles are always 13 hours long (i.e. semi-diurnal) and HW is always at the mid-point of this cycle (i.e.

241 tides are always symmetric). Hence, if there are n extreme events, we expect $n/13$ events to happen at
 242 each hourly band if extreme events are equally likely to occur at any stage of a tidal cycle. However, as
 243 tides are not always semi-diurnal and symmetric, the uniform distribution is not the most suitable null
 244 distribution to represent the null hypothesis. Instead, we propose a “No-Tide-Surge Interaction
 245 distribution” or “No-TSI distribution” as the null distribution. The No-TSI distribution is the *expected*
 246 frequency distribution in the absence of tide-surge interactions. Figure 2 illustrates how this distribution
 247 is obtained. The No-TSI distribution is empirically derived from $T(t)$, the tidal level obtained by applying
 248 UTide to the tide gauge records at each location. It is a distribution that depends on the local tidal
 249 characteristics and hence is location specific. For a given location, the null distribution is generally non-
 250 uniform because the length of the tidal cycle varies. For example, tidal cycles of 14 hours or longer are
 251 relatively rare at Tanjong Pagar, so randomly selected times that occur at 7 hours from the nearest tidal
 252 HW will also be relatively rare (Fig. 3a). This leads to non-uniform sampling of the number of hours from
 253 the nearest tidal HW. The No-TSI distribution corresponds to uniform sampling in time, which is non-
 254 uniform with respect to the number of hours from the nearest tidal HW. Thus, the No-TSI distribution is
 255 obtained by counting the number of tide-gauge observations found at a certain number of hours relative
 256 to HW as illustrated in Fig. 2.

257 The No-TSI distribution allows us to account for the complex mixed tides at each location, which
 258 causes the tidal cycles at the coast to have a period of any duration from 8 to 26 hours (Fig. S4). Let $f(h)$
 259 be the number of tide gauge measurements collected at h hours from HW. Assuming independence
 260 between tide and surge, the probability that an extreme event will be found at h is $p_h = f(h)/\sum_h f(h)$:
 261 the normalized frequency of $f(h)$. Note that p_h is a probability mass function over the domain h : a
 262 function that tells us the probability of an extreme event happening at h is p_h . Letting n be the number of
 263 extreme events that occurred at this tide gauge over its length of records, the No-TSI distribution is simply
 264 $n \cdot p_h$.

265 We can also find the 95% confidence interval of the No-TSI distribution. Assuming that extreme
 266 events are mutually independent, the probability that k_h out of n extremes are found at h hours from HW
 267 follows the binomial distribution $k_h \sim \text{Bin}(n, p_h)$. We compute the 2.5th and 97.5th percentiles of the
 268 binomial distribution at each h to obtain the 95% confidence interval of the No-TSI distribution.

For testing the null hypothesis, a bootstrapping method is used to calculate p -values (Appendix A) with 1,000,000 bootstrap samples. To account for family-wise error rate due to our multiple comparisons at seven locations, we apply the Bonferroni correction to our chosen significance level of 0.05 and require a p -value below $0.05/7 = 0.007$ and $0.05/4 = 0.0125$ to reject the null hypothesis when testing for tide-surge interaction during semi-diurnal and diurnal cycles respectively. This method is chosen over the usual approach of the chi-square test due to our relatively small sample size n . As the chi-square test approximates the binomial distribution of k_h with a normal distribution, a common rule of thumb requires $n \cdot p_h \geq 5$ for a decent approximation. This criterion is not satisfied for most values of h at all seven locations.

3.4 Semi-empirical model

One effect of tide-surge interaction is tidal phase alteration, where surge-caused increase in water depth advances the timing of HW. Our semi-empirical model aims to investigate the first-order effects of tidal phase alteration on the height and timing of residuals due to storm surges driven by wind and the inverse barometer effect. To do so, we first consider the regional context. Singapore and the east coast of Peninsular Malaysia are located within the Sunda Shelf (Fig. 1). The typical bathymetry of 40–80 m in this region of the Sunda shelf terminates at about 700 km away from the coast, declining steeply at the edge of the Sunda Shelf where it borders the South China Sea, which has depths of 4,000 m and deeper. It is within the shallow region that tide-surge interaction is the strongest. Hence, for our semi-empirical model, we estimate the effects of tidal phase alteration due to surges generated within the ocean bounded by the red rectangle in Fig. 1. A rectangular region was chosen for simplicity, with one edge passing through the Tanjong Pagar and Geting gauge locations and the remaining three edges encompassing as much of the shallow shelf as possible. The edges of the rectangle parallel to the Malaysian coast are roughly 833 km long and are separated by a longitude of 6.5° , making the edges perpendicular to the coast roughly 759 km long. To compare the storm surge at the seven tide gauge locations of interest, we assume that the surges at these locations result from forcings over the same region. We model surges as

$$R_{\text{sum}} = R_{\text{baro}} + R_{\text{wind}} + R_{\text{phase}}, \quad (3)$$

296

297 where R_{baro} is the water level response to the inverse barometer effect, R_{wind} is the wind-driven surge
 298 and R_{phase} is the contribution by tidal phase alteration. R_{sum} corresponds to a model estimate of R_{gauge} .

299 To obtain R_{baro} , we assume hydrostatic balance and use the inverse barometer effect by using a
 300 25-hour moving average of pressure:

301

$$302 \quad R_{\text{baro}} = -\frac{\overline{\langle \Delta P \rangle_A}}{\rho g}, \quad (4)$$

303

304 where ΔP is the deviation of sea-level pressure from the global mean, $\langle \Delta P \rangle_A$ represents a spatial average
 305 of ΔP over the ocean within the red rectangle in Fig. 1 and $\overline{\langle \Delta P \rangle_A}$ represents a 25-hour moving average
 306 of $\langle \Delta P \rangle_A$. ρ is the density of seawater, g is the gravitational acceleration and $1/\rho g = 9.9 \times 10^{-5} \text{ m Pa}^{-1}$
 307 (Gregory et al., 2019, Pugh and Woodworth, 2014c).

308 The unique topography of this region with an extensive area that is shallow and relatively uniform
 309 in depth has led us to adopt a simplified version of the sea-level gradient equation to estimate R_{wind} using
 310 wind velocity:

311

$$312 \quad \frac{\partial \zeta}{\partial x} = \frac{\rho_{\text{air}} C_d |\mathbf{W}| \mathbf{W} \cdot \hat{\mathbf{x}}}{\rho g D}, \quad (5)$$

313

314 where we have assumed that the coastal sea is shallow enough to keep only terms with water depth in the
 315 denominator but is deep enough to justify ignoring bottom stress (Pugh and Woodworth, 2014c). In Eq.
 316 (5), ζ is the sea level and x is spatial displacement in a specified direction, making $\partial \zeta / \partial x$ the sea-level
 317 gradient along x . ρ_{air} is the density of air, C_d is the drag coefficient at the sea surface, ρ is the density of
 318 seawater, g is the gravitational acceleration, D is the undisturbed water depth, \mathbf{W} is the wind velocity
 319 vector, and $\hat{\mathbf{x}}$ is a unit vector parallel to x . x is defined to be perpendicular to the edge across Tanjong
 320 Pagar and Geting in Fig. 1. In this region, $g = 9.78 \text{ ms}^{-2}$. Bathymetry influences the height of surges
 321 through the term D in the denominator of Eq. (5), causing shallow regions to experience larger surges
 322 when subject to the same wind forcing.

323 We further assume that ρ_{air} , C_d , ρ and g are spatially and temporally homogeneous over the
 324 bounded region (Gregory et al., 2019) and that C_d is independent of wind speed (Wróbel-Niedzwiecka et
 325 al., 2019). Surges are not only a product of instantaneous winds but are also partially a result of winds
 326 over a past number of hours. To account for the time taken for the winds over the bounded region to cause
 327 surges at the tide gauge locations, we use a 25-hour running average of Eq. (5) to estimate the wind-driven
 328 surge. Based on those assumptions, we estimate R_{wind} by discretising Eq. (5) and numerically integrating
 329 over the 759 km along $\hat{\mathbf{x}}$:

$$331 \quad R_{\text{wind}} = \frac{\rho_{\text{air}} C_d}{\rho g} \int \frac{|\mathbf{W}| \mathbf{W} \cdot \hat{\mathbf{x}}}{D} dx = k \overline{\langle \frac{|\mathbf{W}| \mathbf{W} \cdot \hat{\mathbf{x}}}{D} \rangle}_A, \quad (6)$$

332
 333 where \mathbf{W} is the wind velocity with its zonal (u) and meridional (v) components obtained from the hourly
 334 10m winds of ERA5 (Hersbach et al., 2018), $\hat{\mathbf{x}}$ is a unit vector along x pointing towards the Malaysian
 335 east coast as shown in Fig. 1, $\langle |\mathbf{W}| \mathbf{W} \cdot \hat{\mathbf{x}} / D \rangle_A$ represents a spatial average of $|\mathbf{W}| \mathbf{W} \cdot \hat{\mathbf{x}} / D$ over the ocean
 336 within the red rectangle in Fig. 1, $\overline{\langle |\mathbf{W}| \mathbf{W} \cdot \hat{\mathbf{x}} / D \rangle}_A$ represents a 25-hour moving average of
 337 $\langle |\mathbf{W}| \mathbf{W} \cdot \hat{\mathbf{x}} / D \rangle_A$, $k = \rho_{\text{air}} C_d L_{\text{wind}} / \rho g$ and $L_{\text{wind}} = 759$ km is the distance which Eq. (5) was integrated
 338 over. While most of the constants in k are known, C_d is often used as a final tuning parameter in non-
 339 tidal barotropic models (Zweers et al., 2012, Kurniawan et al., 2015). Using Eq. (3), Eq. (6) and
 340 considering that $|R_{\text{phase}}| \ll |R_{\text{wind}}|$, we fit $\overline{\langle |\mathbf{W}| \mathbf{W} \cdot \hat{\mathbf{x}} / D \rangle}_A$ to $R_{\text{gauge}} - R_{\text{baro}}$. We use a simple linear
 341 regression to obtain the constant k and our estimate for R_{wind} at each location.

342 We obtain our model storm surge as

$$344 \quad R_{\text{surge}} = R_{\text{wind}} + R_{\text{baro}} = k \overline{\langle \frac{|\mathbf{W}| \mathbf{W} \cdot \hat{\mathbf{x}}}{D} \rangle}_A - \frac{\langle \Delta P \rangle_A}{\rho g}. \quad (7)$$

345
 346 To estimate R_{phase} , we consider the influence of depth on the propagation speed of tidal waves.
 347 With the speed of tidal waves given by $c = \sqrt{gD}$ (Pugh and Woodworth, 2014c) and treating R_{surge} as a
 348 perturbation to the undisturbed water depth D , the tide advancement time caused by a change in D due to

349 R_{surge} is

350

351
$$\Delta t = \frac{L_{\text{tide}}}{\sqrt{gD}} - \frac{L_{\text{tide}}}{\sqrt{g(D+R_{\text{baro}}+R_{\text{wind}}/2)}}, \quad (8)$$

352

353 where L_{tide} is the distance travelled by the tidal wave along the shelf. This considers that R_{baro} is the
354 water level response to ΔP averaged over the ocean within the red rectangle in Fig. 1 while R_{wind} is
355 obtained by integrating the sea level gradient over the same area. Hence, we approximate the average
356 depth perturbation due to R_{wind} over this area as $R_{\text{wind}}/2$. We also assume that the tides travel straight
357 towards the coast in the direction of $\hat{\mathbf{x}}$, allowing us to equate $L_{\text{tide}} = L_{\text{wind}}$. We then calculate the effects
358 on residual height due to tide advancement from R_{surge} as $R_{\text{phase}} = T(t + \Delta t) - T(t)$. R_{phase} can be
359 viewed as a phase shift in the tidal levels, where extreme R_{phase} tend to cluster on the rising or falling
360 tides instead of during tidal high or low water (Horsburgh and Wilson, 2007).

361 Finally, we use the procedure described in Sect. 3.2 to obtain the timing of extreme R_{surge} , R_{phase}
362 and R_{sum} relative to HW and plot their frequency distributions. To determine their contributions to tide-
363 surge interaction, the bootstrapping method is used to identify the presence of tide-surge interaction in
364 R_{surge} , R_{phase} and R_{sum} . The frequency distributions of R_{sum} are compared to the frequency
365 distributions of R_{gauge} to evaluate whether R_{sum} can reproduce the tide-surge interaction found in the
366 tide-gauge records.

367 **4 Results and discussion**

368 **4.1 Observed tide-surge interaction**

369 The frequency distributions of R_{gauge} at all seven locations are shown in Fig. 3, all of which deviate
370 significantly from their respective No-TSI distribution and provide evidence of tide-surge interaction at
371 every location. Based on how we have defined extremes, we find that extreme R_{gauge} range from 362 mm
372 at Tanjong Pagar (Fig. 3a) to 1195 mm at Geting (Fig. 3g), with the smallest extremes occurring at the
373 eastern stations and increasing as we travel north. This is expected as the northern part of the coast is

374 more prone to larger storm surges due to tropical depressions (Mohd Anuar et al., 2023). The extremes,
 375 especially the largest extremes at each location, are unlikely to happen close to HW at all seven locations.
 376 This means that while the R_{gauge} exceeding the 99th percentile can occur close to HW, the peak of each
 377 cluster of exceedances is unlikely to be found in the time window close to HW. This also means that the
 378 largest residuals are unlikely to coincide with high tides to form large storm tides. Across the locations,
 379 this time window generally begins 2–3 hours before HW and ends 3–5 hours after HW. Beyond this time
 380 window, the frequency of extreme R_{gauge} increases, giving us frequency distributions that are mostly
 381 bimodal. At the four southernmost stations, we find the primary mode of their frequency distributions
 382 before HW: at -5 hours at Tanjong Pagar (Fig. 3a) and Sedili (Fig. 3c), at -6 hours at Johor Baharu (Fig.
 383 3b) and at -7 hours at Tioman (Fig. 3d). Outside Southeast Asia, similar signals have been found at Port
 384 Otago in New Zealand (Costa et al., 2023), Shijiusuo, Lianyungang and Xiamen along the coast of China
 385 (Feng et al., 2019), Hiron Point at the Bay of Bengal India (Antony and Unnikrishnan, 2013), and
 386 Aberdeen, North Shields, Immingham, Cromer and Sheerness at the North Sea (Horsburgh and Wilson,
 387 2007). At Kuantan, Cendering and Geting (Fig. 3e–3g), the primary mode is found after HW, at +6, +6
 388 and +4 hours respectively. Outside Southeast Asia, such signals have appeared less commonly but have
 389 been found at Onehunga in New Zealand (Costa et al., 2023) and at Kaohsiung and Zhapo in China (Feng
 390 et al., 2019).

391 Comparing our results between the seven tide gauges along Singapore and the east coast of
 392 Peninsular Malaysia, we find a spatial pattern in the tide-surge interaction. At the southernmost stations
 393 of Tanjong Pagar, Johor Baharu and Sedili (Fig. 3a–c), the mass of the frequency distribution is heavily
 394 concentrated around their primary modes, which are found before HW. At Tioman (Fig. 3d), the primary
 395 mode is still found before HW, but the secondary mode has a distinctly heavier weight than the previous
 396 three stations. At Kuantan (Fig. 3e), tide-surge interaction has crossed over to another regime where the
 397 primary mode occurs after HW, but the secondary mode found before HW still carries comparative
 398 weight. At Cendering and Geting (Fig. 3f–g), the northernmost stations, the primary mode after HW is
 399 much heavier than the secondary mode before HW. This spatial pattern can also be seen using the box
 400 plots, which are compiled in Fig. 4a. The tight interquartile range at Tanjong Pagar, Johor Baharu and
 401 Sedili shows that the mass of their frequency distributions is concentrated at -6 to -4 hours relative to

402 HW. The larger interquartile range at Tioman shows that there is a more equal mass between the two
403 modes, with the median at -5 hour and mode at -7 hour revealing that the distribution is still heavier
404 towards the negative values. The opposite is true at Kuantan, with its similar interquartile range to Tioman
405 but with its median at -0.5 and mode at +6 instead. At Cendering and Geting, the lower quartile is closer
406 to HW, showing that the difference in relative mass between the two modes has increased.

407 A transition in the tide-surge interaction characteristic, based on a significant (95% confidence
408 interval) change in the medians from negative to positive values in Fig.4a, happens between Tioman and
409 Geting which are located about 440 km apart. This is a relatively short distance compared to studies that
410 have seen such transition such as 700 km between Zhapo and Xiamen in China (Feng et al., 2019) and
411 1,650 km between Otago and Onehunga in New Zealand (Costa et al., 2023). Feng et al. (2019) suggested
412 that this transition may be related to the ratio between the amplitude of tidal constituents M_2 and K_1 ,
413 where extremes tend towards before HW at locations with larger M_2 and after HW when M_2 is small.
414 We observe the same transition in our study region, where $M_2/K_1 < 1$ at the northernmost stations of
415 Cendering and Geting, $M_2/K_1 = 1$ at Kuantan and $M_2/K_1 > 1$ at the remaining four stations to the south
416 (Table 3).

417 Using the quantitative test (hypothesis testing against the No-TSI distribution), we verify that the
418 p -value of obtaining the frequency distribution from the No-TSI distribution is below the required level
419 at all seven locations, allowing us to reject the null hypothesis that the frequency distribution was drawn
420 from the No-TSI distribution at a significance level of 0.05 (Fig. S5). This provides further evidence
421 supporting the presence of tide-surge interaction during semidiurnal tides at all seven tide gauge locations
422 studied. The presence of tide-surge interaction at these gauges was expected given the shallow regional
423 bathymetry and their proximity of tide-gauges to narrow waterways connecting the Pacific, Indian Ocean,
424 and Java Sea. Locations like the North Sea, English Channel, and some parts along the coast of China
425 where tide-surge interactions have been observed also have similar geographical properties.

426 During diurnal tides, we found no extreme R_{gauge} at Tanjong Pagar, Johor Baharu and Sedili. Few
427 extreme R_{gauge} were found during diurnal tidal cycles at Tioman and Kuantan (Fig. S6a–b), while many
428 were found at Cendering and Geting (Fig. S6c–d). This is expected as Cendering and Geting experience
429 mainly diurnal tides, in contrast to the other locations. The lack of observations at the five other stations

430 is due to the rare occurrence of diurnal tides at these locations, which is shown in Fig. S4. The extreme
 431 R_{gauge} during diurnal tides shares the same spatial characteristics as the extremes during semidiurnal
 432 tides, starting from 410 mm in the South at Tioman (Fig. S6d) and increasing up north to 992 mm at
 433 Geting (Fig. S6g). No extremes are found within two hours of HW. Two observations are available at
 434 Tioman, which are too few to confidently determine the presence of tide-surge interaction even though
 435 both observations were found at least 6 hours after HW. The same can be said for Kuantan, where seven
 436 observations are available and were mostly found at least 6 hours after HW. Nonetheless, we calculate
 437 their p -values and compare them to $0.05/4 = 0.0125$. We find that their p -values are insufficient to
 438 reject the null hypothesis that the observed frequency distribution was drawn from the No-TSI distribution
 439 at a significance level of 0.05 and fails to provide evidence of tide-surge interaction during diurnal tidal
 440 cycles at these two locations. The results at these two locations are more likely due to a lack of sufficient
 441 data than an indication of the absence of any tide-surge interaction, and we expect to see tide-surge
 442 interaction based on the properties of the geography discussed earlier. At Cendering and Geting, we
 443 continue to see the pattern where extreme R_{gauge} are unlikely to happen close to HW. This leads to a
 444 bimodal distribution with the primary modes at both locations found after HW, like their semidiurnal
 445 counterparts. The mode is 14 hours after HW at Cendering and 13 hours after HW at Geting. Respective
 446 p -values provide evidence of tide-surge interaction at both locations (Fig. S7) as expected at these
 447 locations.

448 4.2 Semi-empirical model results

449 We obtain R_{surge} by fitting $\overline{\langle |\mathbf{W}| \mathbf{W} \cdot \hat{\mathbf{x}} / D \rangle_A}$ to $R_{\text{gauge}} - R_{\text{baro}}$ as described in Sect. 3.4. R_{surge} has a
 450 correlation of 0.7–0.8 with the tide gauge residuals (Fig. S8). This corresponds to an explained variance
 451 (coefficient of determination) of 0.5–0.6. This suggests R_{surge} is an adequate proxy of storm surges.

452 We obtain the timing of extreme R_{surge} as a frequency distribution using the procedure described
 453 in Sect. 3.2 and compare it to its No-TSI distribution using hypothesis testing to determine whether there
 454 is any signal of tide-surge interaction in R_{surge} . The reason for doing so is to show that the observed tide-
 455 surge interaction between R_{gauge} and tide is not caused by any correlation between wind and tide or wind

456 and atmospheric sea level pressure, which are generated by independent processes. The validation of this
457 assumption would imply that the observed dependence between R_{gauge} and tide is not caused by possible
458 correlation to a common third independent variable, but that tide-surge interaction is indeed present. We
459 find that the resulting frequency distributions for R_{surge} do not deviate significantly from their No-TSI
460 distribution and provide no evidence of dependence between R_{surge} and tide (Fig. S9–S12), indicating
461 the absence of such a confounding variable.

462 To estimate the influence of tidal phase modulation, we compute Δt using Eq. (8) and then
463 calculate $R_{\text{phase}} = T(t + \Delta t) - T(t)$ (Sect. 3.4). We apply the procedure of Sect. 3.2 to obtain the
464 extremes of R_{phase} and find a clear dependence between R_{phase} and tide (Fig. S13–S16). During semi-
465 diurnal tidal cycles, extreme values of R_{phase} are mostly found 2–4 hours before HW at all seven locations
466 (Fig. S13). During diurnal cycles, extreme values are mostly found 3–5 hours before HW (Fig. S15). As
467 with R_{gauge} and R_{wind} , we found no extremes during diurnal cycles at Tanjong Pagar, Johor Baharu and
468 Sedili.

469 The prevalence of extreme R_{phase} within a narrow window of time relative to HW is due to R_{phase}
470 being largest at one-fourth of a tidal cycle before HW, as illustrated in Fig. S17. As the natural period of
471 a semi-diurnal tidal cycle is about 12–13 hours, a sinusoidal tidal waveform has the steepest gradients
472 about 3 hours from its local maxima. This results in the tidal waveform having the greatest difference
473 from a slightly horizontally displaced copy at close to 3 hours from HW. Horsburgh and Wilson (2007)
474 describe this mechanism in detail. However, extreme values of R_{phase} are not found at 6 hours before
475 HW during diurnal tides. This is because a sinusoidal wave with amplitude A and frequency ω has a
476 gradient that is proportional to the product $A\omega$. Since semidiurnal components of tides have about twice
477 the frequency of their diurnal counterparts, diurnal constituents need to have at least twice the amplitude
478 of semidiurnal constituents to have the same or stronger influence on R_{phase} . The tidal form factor F ,
479 which computes the ratio between the amplitudes of the main diurnal and semidiurnal constituents, can
480 provide a measure of this influence. While the tides at Cendering and Geting are mainly diurnal, the tidal
481 form factors at both locations are lower than 2 which indicates that the diurnal constituents have

482 amplitudes less than twice that of the semidiurnal constituents (Table 3). Therefore, the semidiurnal signal
483 has a stronger influence on the timing of extreme R_{phase} .

484 The frequency distributions of R_{sum} at the seven locations during semidiurnal tidal cycles are
485 shown in Fig. 5. The frequency distributions and p -values for R_{sum} suggest the presence of tide-surge
486 interaction at Tanjong Pagar, Johor Baharu, Sedili, Tioman, Kuantan and Cendering (Fig. 5a–f and S18a–
487 f). No significant interaction is identified at Geting (Fig. 5g and S15g). This can also be seen in Fig. 4b
488 where the interquartile range of the frequency distributions at Geting do not deviate from zero while the
489 interquartile range at the other six locations do. Figure 5 reveals that our semi-empirical model predicts
490 frequency distribution of R_{sum} at all seven locations to have a single mode as opposed to the bimodal
491 frequency distribution of the tide gauge residuals. At the six locations where R_{sum} provides an indication
492 of tide-surge interaction, the modes of their frequency distributions of R_{sum} lie within 2–4 hours before
493 HW, following R_{phase} . During diurnal tidal cycles, we find evidence of tide-surge interaction only at
494 Cendering (Fig. S19c and 20c) while no evidence of tide-surge interactions can be seen at Tioman,
495 Kuantan and Geting (Fig. S19a, b, d, S20a, b, d). As with their R_{gauge} counterparts, the hypothesis testing
496 results at Tioman and Kuantan are likely due to a lack of sufficient observations (Fig. S19a–b). The result
497 at Geting, which is negative for tide-surge interactions, is likely due to its relatively weaker diurnal
498 constituents. This can be seen from the tidal form factor F in Table 3, where the form factor of 1.56 at
499 Geting is lower than 1.90 at Cendering which tested positive for tide-surge interactions.

500 We find that R_{phase} can significantly influence the distribution of the extreme values of R_{sum} ,
501 indicating that the process of tidal phase alteration—where surges perturb the depth of the water body
502 and influences the propagation speed of the tide—produces a significant and measurable tide-surge
503 interaction at six locations. This is despite R_{phase} contributing to <1% of the variance of R_{sum} at all seven
504 tide gauge locations (Fig. S21). By an alternative metric, the ratio between the standard deviation of
505 R_{phase} and the standard deviation of R_{surge} is only 0–2%. Thus, while the magnitude of R_{sum} is
506 effectively fully dependent on R_{surge} , the timing of its largest values is dependent on R_{phase} , indicating
507 the significant contribution of tidal phase alteration to tide-surge interaction. Our findings complement
508 those of Chen et al. (2012), who found that the influence of tide-surge interactions on large surges is

negligible, although tide-surge interaction may alter the time of tidal high and low water. Accounting for tide-surge interaction would be important in applications such as forecasting where timing is important and has been found to improve water level predictions in this region and other parts of the world (Antony et al., 2020; Fernández-Montblanc et al., 2019; Kurniawan et al., 2015; Idier et al., 2012).

Comparing Fig 4b to 4a, our semi-empirical model (Fig. 4b and 5) is unable to accurately predict all the characteristics of tide-surge interaction found in R_{gauge} (Fig. 3 and 4a). At Tanjong Pagar, Johor Baharu, Sedili and Tioman, extreme residuals typically occur even earlier than what our model suggests. Tidal phase alteration shifts the timings of extreme residuals towards times where tides are rising or falling the quickest, and no further. Our model is also unable to produce the bimodal distribution found in the tide gauge data illustrated in Fig. 3 and fails to produce statistically significant tide-surge interaction at Geting. This suggests that the mechanism of tidal phase alteration cannot fully explain the observed tide-surge interaction and that additional explanations are required to fully account for the observations.

One possible contributor is that shallower water during low tides can result in higher surges from near-shore winds (Pugh and Woodworth, 2014c). Changes in tides due to tidal phase alteration can affect the height of surges through Eq. (5), while surges further contribute to tidal phase alteration through Eq. (8) causing the mutually interacting process of mutual phase alteration between tides and surges. Kurniawan et al. (2014) found that the tidal cycle does influence non-tidal residuals in this region. This could result in a further shift of the model extremes towards tidal low water, which would be closer to the observed tide-surge interaction. The impact of non-linear effects resulting from bottom friction and momentum advection also cannot be overlooked in coastal areas and are significant in this region (Kurniawan et al., 2015). We were not able to consider the effects of water flow between the Pacific and Indian Ocean through the Singapore and Johor Strait on the results at Tanjong Pagar and Johor Baharu. We also could not account for the tide-surge-river interactions at Sedili, the presence of Tioman island at Tioman, and how the Gulf of Thailand affects tide-surge interactions at the northern tide gauges. Our semi-empirical model can reveal macroscopic properties of tide-surge interactions but is unable to reveal detailed spatial and temporal properties at high resolution like alternative numerical models. To reveal such details, the use of dynamical models or partial differential equation solvers would be needed. For instance, Kurniawan et al. (2015) and Tay et al. (2016) used a multi-scale depth-integrated hydrodynamic

537 model that simulated hydrodynamics at a higher spatial and temporal resolution and found significant
538 contribution in the order of 10 cm to non-tidal residuals by tide-surge interactions. However, such
539 numerical models are complex, difficult to tune, and computationally intensive. While it does not replace
540 hydrodynamical models, our semi-empirical model offers theoretical insights by providing a clear and
541 transparent explanation of tidal phase alteration and its impact at a low computational cost.

542 The semi-empirical model is less applicable elsewhere because it has been designed for the study
543 region. However, the semi-empirical model could be modified for other coastlines situated along a
544 shallow shelf. For instance, the physical characteristic of our study region—a semi-enclosed shallow
545 region leading out to steep depths—can be found on a smaller spatial scale at the Yellow Sea and North
546 Sea and our semi-empirical model may find similar success there.

547 Testing our No-TSI distribution against the uniform distribution, we found false positive signals
548 for tide-surge interactions in R_{surge} at Tanjong Pagar and Johor Baharu and in R_{sum} at Geting when using
549 the uniform distribution. Using the No-TSI distribution at locations that have similar frequency
550 distributions such as Green Island in New Zealand (Costa et al., 2023), Newlyn in UK (Haigh et al., 2010),
551 and several locations in China (Feng et al., 2019) may lead to a different conclusion regarding the
552 existence of tide-surge interactions.

553 The existence of strong tide-surge interactions in this region discourages the use of the revised
554 joint probability method for estimation of sea level extremes, which works well in locations with short
555 records but tends to overestimate return levels at locations with strong tide-surge interactions (Arns et al.,
556 2020; Olbert et al., 2013; Haigh et al., 2010; Tawn, 1992; Tawn and Vassie, 1989). The use of skew surge
557 for the estimation of extremes may be more suitable than surge or residuals for this region (Williams et
558 al., 2016).

559 **5 Conclusions**

560 We have introduced the No-TSI distribution to be used in determining the presence of tide-surge
561 interaction. The No-TSI distribution can account for irregular tidal cycles that can lead to non-uniform
562 sampling with respect to the number of hours from HW. Hence, the No-TSI distribution is generally not

563 a uniform distribution. When determining the presence of tide-surge interaction, the observed frequency
564 distribution should be compared to the No-TSI distribution instead of a uniform distribution.

565 Analysis of tide gauge records using the No-TSI distribution provides evidence of tide-surge
566 interaction at all seven tide-gauge locations along Singapore and the east coast of Peninsular Malaysia.
567 The observed interactions have a smooth spatial dependence along the coastline. During semi-diurnal
568 tidal cycles at the southernmost location of Tanjong Pagar, extreme residuals are mostly found around 5
569 hours before tidal HW with a much smaller number of extremes occurring after HW. Moving northwards,
570 similar patterns are found at Johor Baharu and Sedili, until we reach Tioman where extremes are mostly
571 found before HW but many extremes can also be found after HW. Northwards from Kuantan, most
572 extremes are found after HW. The strong tide-surge interaction in this region suggests that return levels
573 should be estimated using skew surge, not hourly residuals.

574 To investigate the contribution of tidal phase alteration, we proposed a semi-empirical model. We
575 used 10 m winds from ERA5 to estimate the effects of tidal phase alteration. At the six southern stations
576 of Tanjong Pagar, Johor Baharu, Sedili, Tioman, Kuantan and Cendering, we found that R_{phase} —the
577 residual component caused by the advancement of tidal HW due to surges—can significantly alter the
578 timing of extremes despite being responsible for less than 1% of the variance of the total residual. This
579 demonstrates the effects of tidal phase alteration on the timing of extreme residuals.

580 Our model has explored one of the underlying mechanisms behind tide-surge interaction but is
581 not designed to forecast water level or extreme events. A forecast model would require much more
582 accurate modelling of storm surge. The inclusion of other underlying mechanisms of tide-surge
583 interaction, such as the effect of tidal level on surge generation, would also be beneficial. Knowledge of
584 the interplay between tide-surge interaction and extreme sea levels can aid in the design of effective
585 strategies for coastal planning, risk assessment, and mitigation measures, and will benefit from more
586 comprehensive analyses. When studying extreme sea level in Southeast Asia, the relatively short length
587 of available tide gauge records poses a challenge, providing a focus for further research.

588 Appendix A: Calculating p -value with bootstrapping

589 Here, our objective is to determine whether the *frequency distribution* obtained in Sect. 3.2 is drawn from
590 the No-TSI distribution. To do so, we calculate the p -value: the probability of obtaining distributions
591 from the No-TSI distribution that are at least as extreme as the *frequency distribution*. We can estimate
592 this probability by considering the following: if we draw a random sample from the No-TSI distribution,
593 the probability of drawing an outcome that is equally as probable or less probable than the *frequency*
594 *distribution* is, by the definition of p -values, equal to p . Hence, we can obtain a good estimate of the p -
595 value by drawing many samples from the No-TSI distribution and calculating the ratio of samples that
596 are equally as probable or less probable than the *frequency distribution* to be drawn from the No-TSI
597 distribution.

598 To obtain one bootstrap sample, following the notation in Sect 3.3, we draw one sample of size n
599 from the normalised No-TSI distribution p_h . To proceed, we need to calculate the probability of obtaining
600 this specific outcome. Labelling this outcome as \mathbf{k} , \mathbf{k} follows a multinomial distribution with probability
601 given by $p_{\{\mathbf{k}\}} = \frac{n!}{\prod_h k_h!} \prod_h p_h^{k_h}$ where k_h is the number of times (out of n times) each possible h is drawn.
602 We can also compute $p_{\{\mathbf{k}^{(0)}\}}$, the probability of obtaining the *frequency distribution* from the No-TSI
603 distribution, in the same way using the multinomial distribution. After obtaining 1,000,000 bootstrap
604 samples and calculating their probabilities, we can achieve a good estimate of the p -value as

$$605 \quad p = \frac{\text{\# of samples where } p_{\{\mathbf{k}\}} \leq p_{\{\mathbf{k}^{(0)}\}}}{1,000,000}.$$

606

607

608 *Code and data availability.* The hourly tide gauge data can be downloaded from the University of Hawaii Sea Level
609 Center (UHSLC) at <https://uhslc.soest.hawaii.edu/data/?rq> (Caldwell et al., 2001). The UTide MATLAB functions
610 can be downloaded from [https://www.mathworks.com/matlabcentral/fileexchange/46523-utide-unified-tidal-](https://www.mathworks.com/matlabcentral/fileexchange/46523-utide-unified-tidal-analysis-and-prediction-functions)
611 [analysis-and-prediction-functions](https://www.mathworks.com/matlabcentral/fileexchange/46523-utide-unified-tidal-analysis-and-prediction-functions) (Codiga, 2011). The ERA5 hourly data can be downloaded from
612 <https://doi.org/10.24381/cds.adbb2d47> (Hersbach et al., 2018). The bathymetry data can be downloaded from
613 GEBCO at <https://download.gebco.net/> (GEBCO Compilation Group, 2023). The analysis code used to produce
614 the figures and tables can be downloaded from <https://doi.org/10.5281/zenodo.12721300>.

615

616 *Author contributions.* ZYK: conceptualisation; data curation; formal analysis; investigation; methodology;
617 software; visualisation; writing – original draft preparation; writing – review and editing. BSG: conceptualisation;
618 investigation; methodology; writing – review and editing. DS: writing – review and editing. ADS:
619 conceptualisation; writing – review and editing. BPH: funding acquisition; supervision (supporting); writing –
620 review and editing. JD: funding acquisition; supervision (supporting); writing – review and editing. LYC: funding
621 acquisition; project administration; resources; supervision (lead); conceptualisation; investigation; methodology;
622 writing – review and editing.

623

624 *Competing interests.* The authors declare that they have no conflict of interest.

625

626 *Acknowledgements.* This Research is supported by the National Research Foundation, Singapore, and National
627 Environment Agency, Singapore under the National Sea-Level Programme Funding Initiative (Award No. USS-
628 IF-2020-3 and USS-IF-2020-1) and the Ministry of Education, Singapore, under its MOE AcRF Tier 3 Award
629 MOE2019-T3-1-004. Any opinions, findings, conclusions, or recommendations expressed in this material are those
630 of the author(s) and do not reflect the views of the National Research Foundation, Singapore, and the National
631 Environment Agency, Singapore. This work comprises EOS contribution number 606.

632

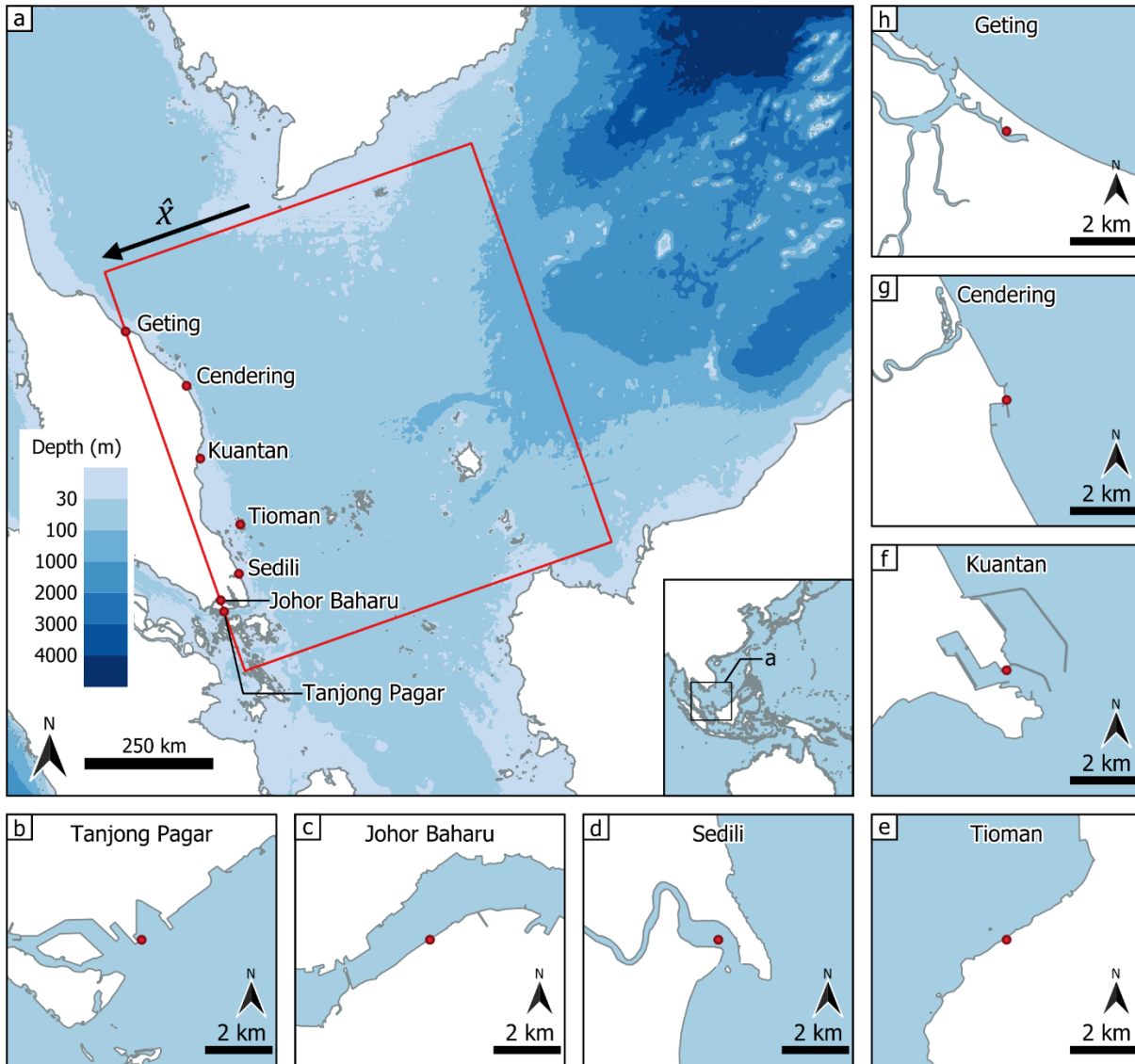


Figure 1: (a) Bathymetry of the region of interest of this study, obtained from GEBCO, the General Bathymetric Chart of the Oceans (GEBCO Compilation Group, 2023). The inset shows the location of this region within East and Southeast Asia. The seven tide gauge stations analysed are marked in red circles. The red rectangle denotes the region where 10 m winds and mean sea level pressure are considered when calculating R_{surge} (Sect. 3.4). The region is roughly a rectangle of 759 km by 833 km. The unit vector \hat{x} used in Eq. (5)–(7) is shown in the figure. (b–h) Close up of the seven tide gauge locations (OpenStreetMap contributors, 2017).

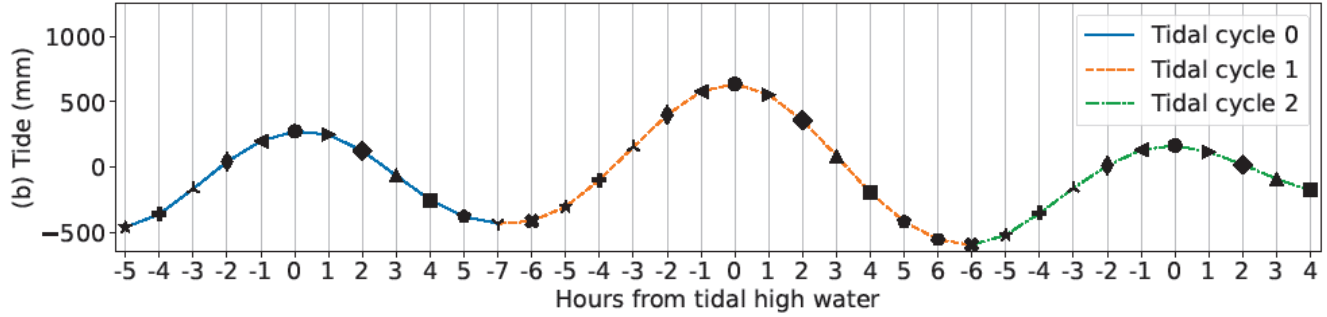
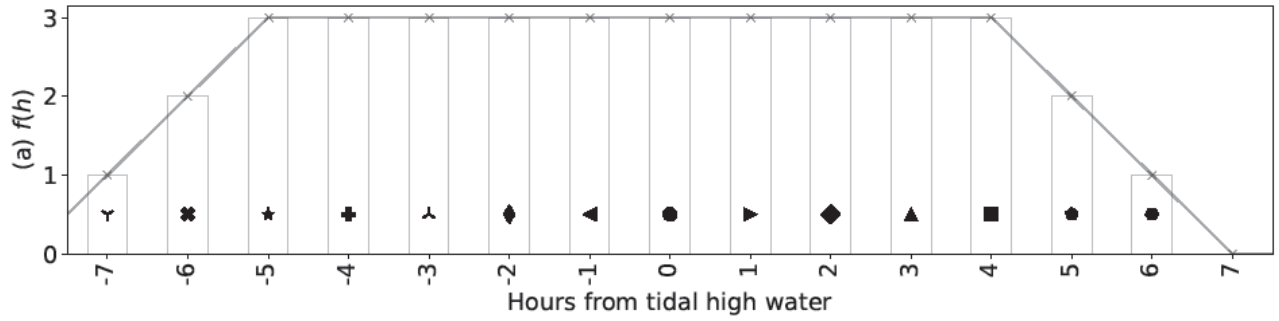


Figure 2: An example of how the No-TSI distribution is obtained, using three tidal cycles at Tanjong Pagar tide gauge station between 1 and 2 Jan 1989 (GMT). The number of hourly measurements made at h hours from HW are counted and denoted as $f(h)$, the No-TSI distribution before normalization and scaling by the number of events (Sect. 3.3). In this example, if an extreme residual can occur at any hour with equal probability, it will be 3 times more likely to happen at HW than at 7 hours before HW. This is observed from (b) where $-5 \leq h \leq 4$ occur thrice, $h = -6$ and $h = 5$ occur twice, and $h = -7$ and $h = 6$ occur once, resulting from the three irregular tidal cycles.

Number of R_{gauge} extremes found at x hours from nearest tidal high water

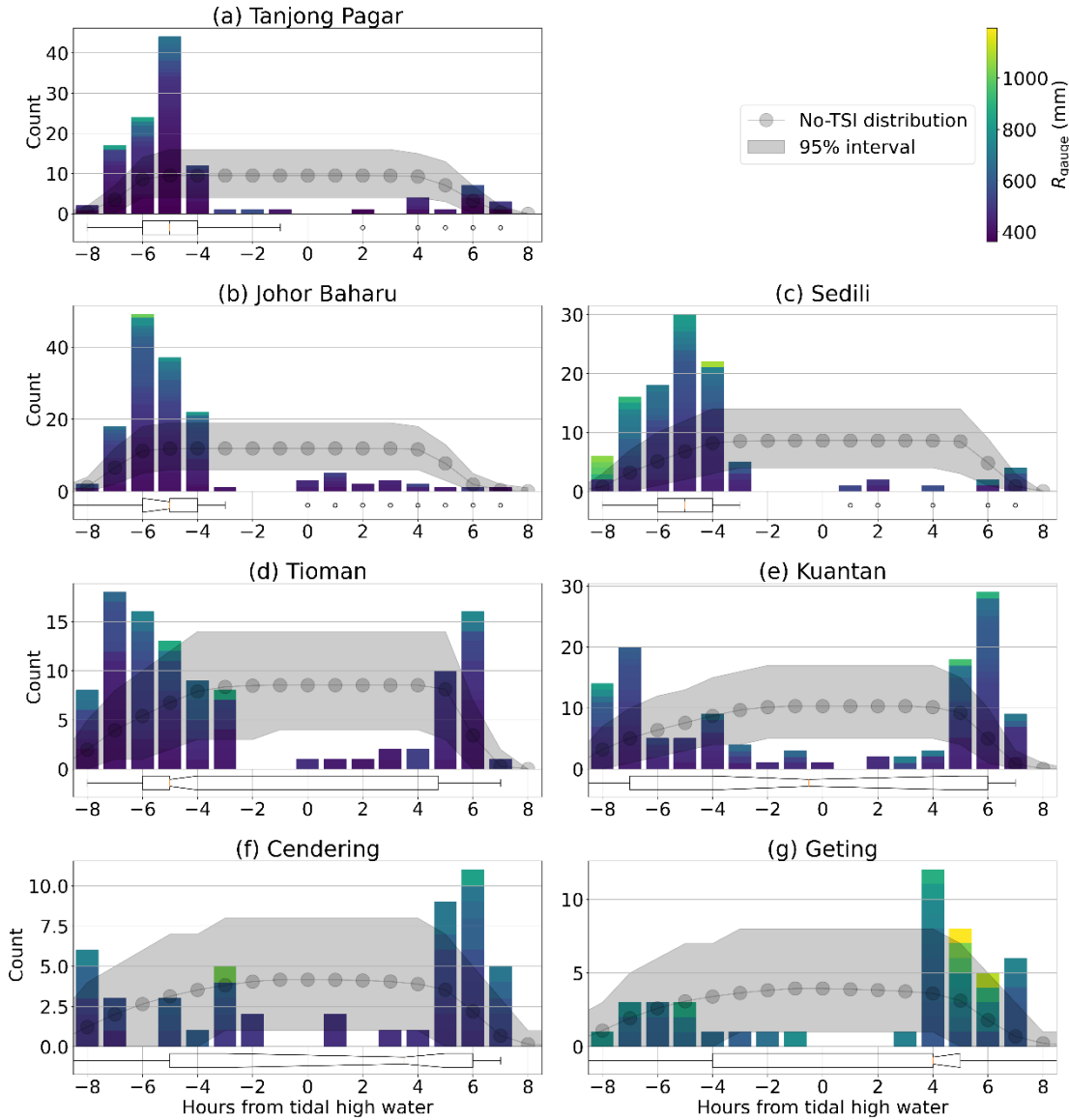


Figure 3: Frequency distribution—the number of extreme events that have occurred at a certain number of hours relative to HW—of extreme residuals (R_{gauge}) during semidiurnal tidal cycles (Sect. 3.2). The plots are truncated at ± 8 hours from HW. The frequency distribution is compared to the No-TSI distribution, shown in grey, to determine the presence of tide-surge interaction (Sect. 3.3). Summary statistics of the frequency distribution are shown using the horizontal notched box plot (Sect. 3.2). The whiskers of the box plot at (b) Johor Baharu, (e) Kuantan, (f) Cendering and (g) Geting extend beyond ± 8 hours from HW, and their full extent is shown in Figure 4.

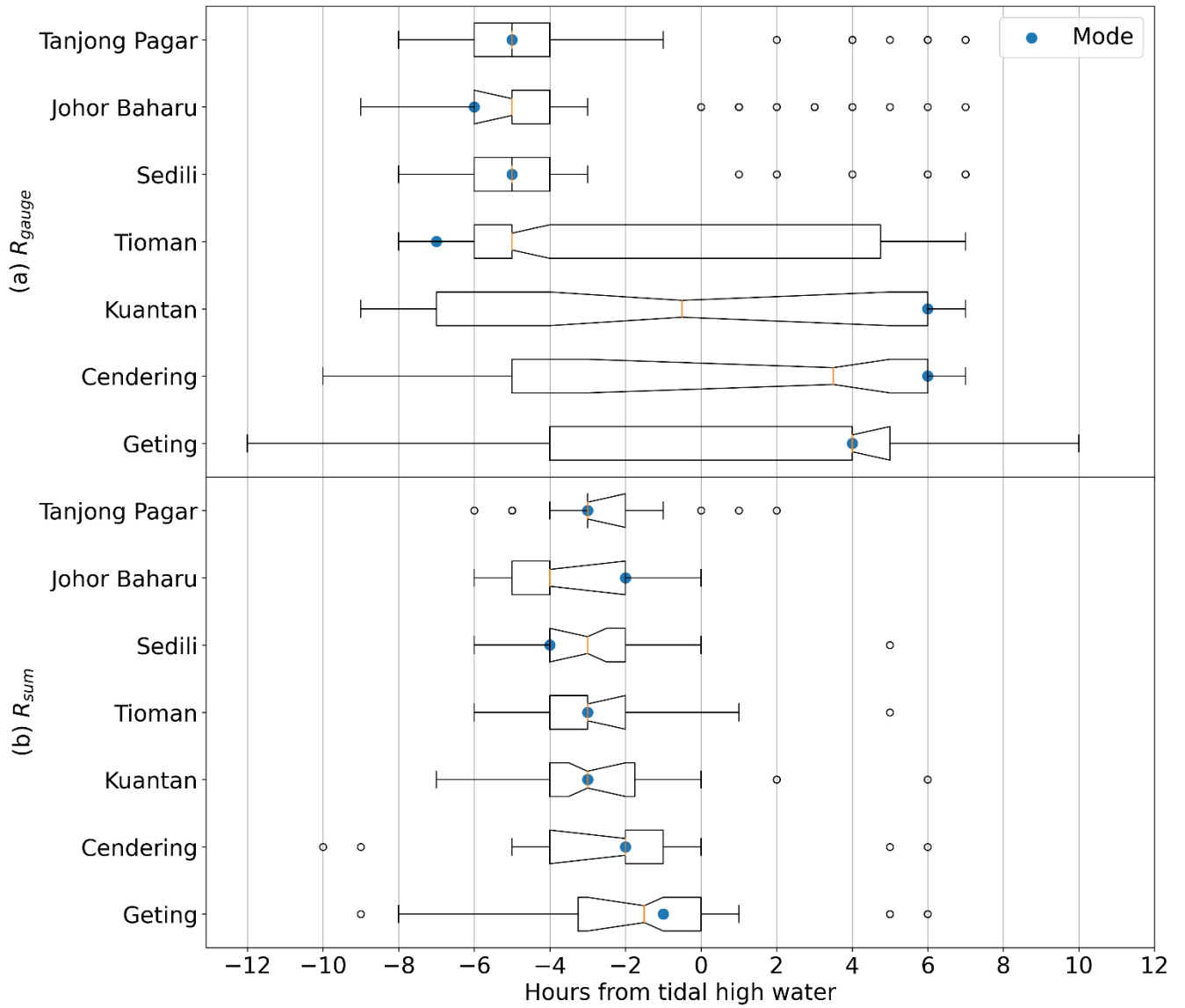


Figure 4: Compilation of the box plots in Fig. 3 and Fig. 5. Results presented in Fig. 3 on the timing of extreme residuals are compiled in subplot (a) and results presented in Fig. 5 on extreme values of R_{sum} are compiled in subplot (b). The box plots illustrate summary statistics of the distribution $k^{(0)}$ at each location, where orange lines indicate the medians, notches indicate the 95% confidence interval of the medians, blue circles indicate the modes, notched rectangles indicate the interquartile range (IQR), whiskers indicate a range that extends up to $1.5 \times \text{IQR}$ from the limits of the IQR, and black circles indicate outliers outside this range.

Number of R_{sum} extremes found at x hours from nearest tidal high water

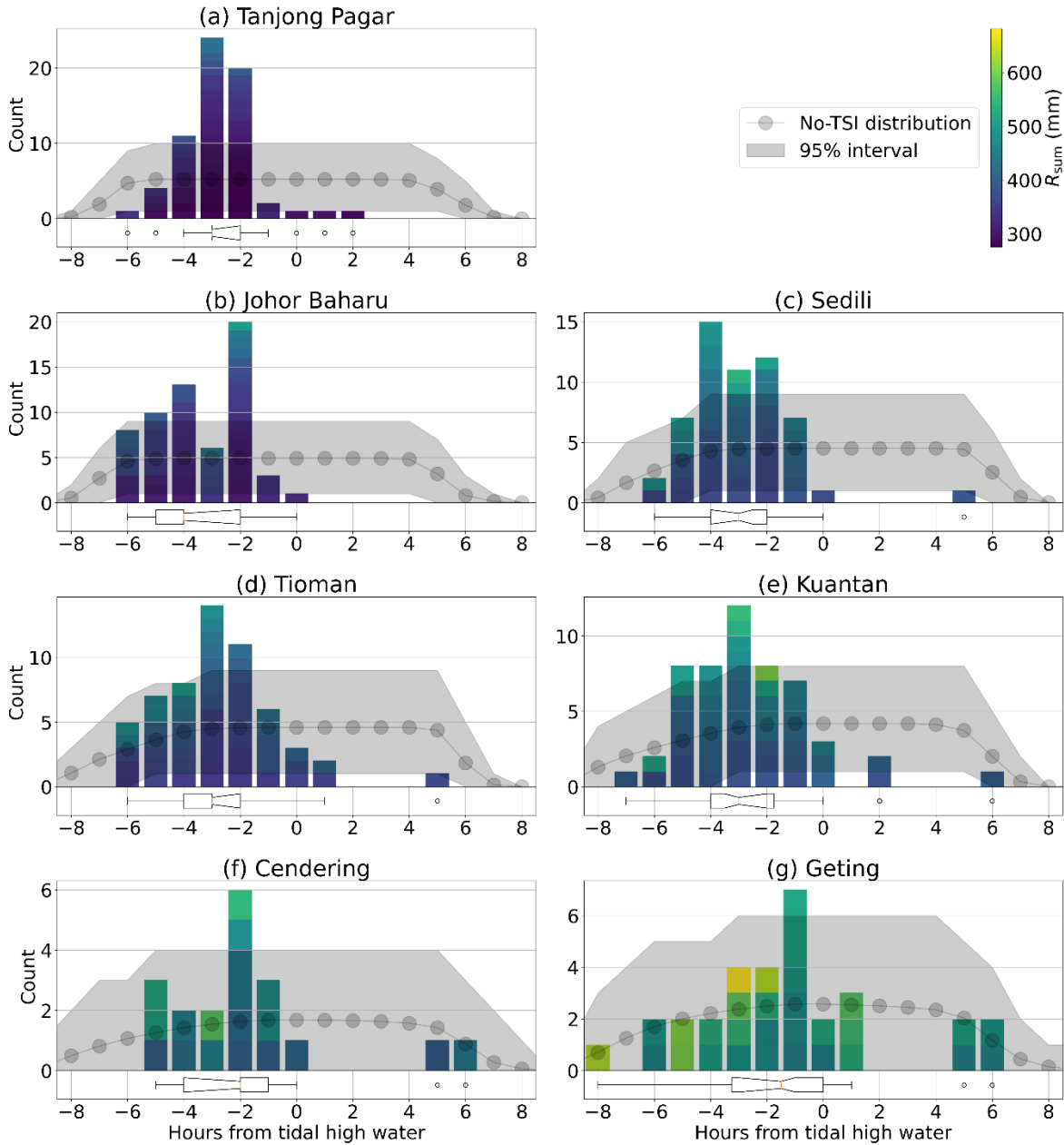


Figure 5: The frequency distribution for extreme values of R_{sum} and the No-TSI distribution during semidiurnal tidal cycles, truncated at ± 8 hours from tidal HW. Truncated horizontal notched box plots illustrate some summary statistics of the frequency distribution, and their full extents are shown in Fig. 4.

676 **Table 1: Data availability of the tide gauges used in this study. Completion rate is the percentage of**
677 **usable hourly observations out of the duration of records. Usable rate is the percentage of usable**
678 **observations subtracting 1-year moving averages (Sect. 3.1).**

Location	Latitude	Longitude	Start	End	Years	Completion (%)	Usable (%)
Tanjong Pagar	1.262	103.853	1988-01-01	2018-12-30	31.0	95.42	89.24
Johor Baharu	1.462	103.792	1983-12-19	2013-12-31	30.0	95.02	87.11
Sedili	1.932	104.115	1986-12-23	2015-12-09	29.0	98.08	98.08
Tioman	2.807	104.140	1985-11-13	2015-12-31	30.1	96.47	89.22
Kuantan	3.975	103.430	1983-12-22	2015-12-31	32.0	98.70	98.70
Cendering	5.265	103.187	1984-11-01	2015-11-30	31.1	96.58	90.58
Geting	6.227	102.107	1986-12-17	2015-12-31	29.0	99.14	99.14

679

680 **Table 2: Standard deviation and certain key quantiles of detrended water level, $X(t) - Z(t)$, at the**
681 **seven tide gauges (mm).**

Location	Standard Deviation	Min	Lower quartile	Median	Upper quartile	Max
Tanjong Pagar	713	-2011	-539	45	578	1919
Johor Baharu	767	-2267	-575	67	596	2007
Sedili	569	-1703	-397	49	422	1843
Tioman	644	-1984	-436	6	457	2045
Kuantan	650	-2050	-440	-27	446	2173
Cendering	525	-1665	-371	-22	368	1843
Geting	321	-937	-238	-26	217	1412

682

683 **Table 3: Summary of the tidal characteristics at the study locations including tidal range, four tidal**
 684 **constituents (K_1 , O_1 , M_2 , S_2), and the tidal form factor (F). Units, where applicable, are in metres**
 685 **(m). The diurnal tidal range is the difference between mean higher high water and mean lower low**
 686 **water, and is also referred to as the great diurnal tidal range or great diurnal range (NOAA, 2000).**
 687 **Maximum tidal range is the greatest difference between higher high and lower low water within a**
 688 **single day, and is much larger than the diurnal tidal range.**

Location	Tidal Range		K_1	O_1	M_2	S_2	F
	Diurnal	Max					
Tanjong Pagar	2.2	3.3	0.31	0.30	0.80	0.32	0.54
Johor Baharu	2.4	3.6	0.31	0.31	0.88	0.34	0.50
Sedili	1.8	2.8	0.35	0.31	0.56	0.16	0.91
Tioman	2.1	3.5	0.46	0.34	0.60	0.19	1.03
Kuantan	2.0	3.6	0.53	0.36	0.53	0.18	1.26
Cendering	1.5	2.7	0.49	0.31	0.30	0.12	1.90
Geting	0.8	1.4	0.25	0.13	0.17	0.08	1.56

689

690 **References**

- 691 Abd Razak, W. A. J., Ramli, M. Z., Baharim, N. B., Shubri, S. M., Zakaria, J., Harris, M. F., Ali, A., and
692 Ariffin, E. H.: Storm surge induced by 2019 Tropical Storm Pabuk and impact on the shoreline in
693 Kuala Nerus Terengganu, east coast of Peninsular Malaysia, *Regional Studies in Marine Science*,
694 74, 103–536, <https://doi.org/10.1016/j.rsma.2024.103536>, 2024.
- 695 Antony, C. and Unnikrishnan, A. S.: Observed characteristics of tide-surge interaction along the east coast
696 of India and the head of Bay of Bengal, *Estuarine, Coastal and Shelf Science*, 131, 6–11,
697 <https://doi.org/10.1016/j.ecss.2013.08.004>, 2013.
- 698 Antony, C., Unnikrishnan, A. S., Krien, Y., Murty, P. L. N., Samiksha, S. V., and Islam, A. K. M. S.:
699 Tide–surge interaction at the head of the Bay of Bengal during Cyclone Aila, *Regional Studies in*
700 *Marine Science*, 35, 101–133, <https://doi.org/10.1016/j.rsma.2020.101133>, 2020.
- 701 Arns, A., Wahl, T., Wolff, C., Vafeidis, A. T., Haigh, I. D., Woodworth, P., Niehüser, S., and Jensen, J.:
702 Non-linear interaction modulates global extreme sea levels, coastal flood exposure, and impacts,
703 *Nature Communications*, 11, 1918, <https://doi.org/10.1038/s41467-020-15752-5>, 2020.
- 704 Buchanan, M. K., Kopp, R. E., Oppenheimer, M., and Tebaldi, C.: Allowances for evolving coastal flood
705 risk under uncertain local sea-level rise, *Climatic Change*, 137, 347–362,
706 <https://doi.org/10.1007/s10584-016-1664-7>, 2016.
- 707 Calafat, F. M., Wahl, T., Tadesse, M. G., and Sparrow, S. N.: Trends in Europe storm surge extremes
708 match the rate of sea-level rise, *Nature*, 603, 841–845, [https://doi.org/10.1038/s41586-022-04426-](https://doi.org/10.1038/s41586-022-04426-5)
709 [5](https://doi.org/10.1038/s41586-022-04426-5), 2022.
- 710 Caldwell, P. C., Merrifield, M. A., and Thompson, P. R.: Sea level measured by tide gauges from global
711 oceans as part of the Joint Archive for Sea Level (JASL) since 1846,
712 <https://doi.org/10.7289/V5V40S7W>, 2001.
- 713 Cannaby, H., Palmer, M. D., Howard, T., Brichenno, L., Calvert, D., Krijnen, J., Wood, R., Tinker, J.,
714 Bunney, C., Harle, J., Saulter, A., O'Neill, C., Bellingham, C., and Lowe, J.: Projected sea level
715 rise and changes in extreme storm surge and wave events during the 21st century in the region of
716 Singapore, *Ocean Science*, 12, 613–632, <https://doi.org/10.5194/os-12-613-2016>, 2016.

717 Chen, H., Tkalich, P., Malanotte-Rizzoli, P., and Wei, J.: The forced and free response of the South China
 718 Sea to the large-scale monsoon system, *Ocean Dynamics*, 62, 377–393,
 719 <https://doi.org/10.1007/s10236-011-0511-7>, 2012.

720 Codiga, D.: Unified tidal analysis and prediction using the UTide Matlab functions, Tech. rep., Graduate
 721 School of Oceanography, University of Rhode Island,
 722 <https://doi.org/10.13140/RG.2.1.3761.2008>, 2011.

723 Costa, W., Bryan, K. R., Stephens, S. A., and Coco, G.: A regional analysis of tide-surge interactions
 724 during extreme water levels in complex coastal systems of Aotearoa New Zealand, *Frontiers in*
 725 *Marine Science*, 10, <https://www.frontiersin.org/articles/10.3389/fmars.2023.1170756>, 2023.

726 Diaz, D. B.: Estimating global damages from sea level rise with the Coastal Impact and Adaptation Model
 727 (CIAM), *Climatic Change*, 137, 143–156, <https://doi.org/10.1007/s10584-016-1675-4>, 2016.

728 Dixon, M. J. and Tawn, J. A.: Extreme Sea-levels at the UK A-class Sites: Site-by-site Analyses,
 729 Proudman Oceanographic Laboratory Internal Document No. 65,
 730 https://ntslf.org/sites/ntslf/files/pdf/other_reports/id65.pdf, 1994.

731 Feng, J., Jiang, W., Li, D., Liu, Q., Wang, H., and Liu, K.: Characteristics of tide–surge interaction and
 732 its roles in the distribution of surge residuals along the coast of China, *Journal of Oceanography*,
 733 75, 225–234, <https://doi.org/10.1007/s10872-018-0495-8>, 2019.

734 Fernández-Montblanc, T., Vousedoukas, M. I., Ciavola, P., Voukouvalas, E., Mentaschi, L., Breyiannis,
 735 G., Feyen, L., and Salamon, P.: Towards robust pan-European storm surge forecasting, *Ocean*
 736 *Modelling*, 133, 129–144, <https://doi.org/10.1016/j.ocemod.2018.12.001>, 2019.

737 GEBCO Compilation Group: The GEBCO_2023 Grid – a continuous terrain model of the global oceans
 738 and land, NERC EDS British Oceanographic Data Centre NOC [data set],
 739 <https://doi.org/10.5285/f98b053b-0cbc-6c23-e053-6c86abc0af7b>, 2023.

740 Gregory, J. M., Griffies, S. M., Hughes, C. W., Lowe, J. A., Church, J. A., Fukimori, I., Gomez, N., Kopp,
 741 R. E., Landerer, F., Cozannet, G. L., Ponte, R. M., Stammer, D., Tamisiea, M. E., and van de Wal,
 742 R. S. W.: Concepts and Terminology for Sea Level: Mean, Variability and Change, Both Local
 743 and Global, *Surveys in Geophysics*, 40, 1251–1289, [https://doi.org/10.1007/s10712-019-09525-](https://doi.org/10.1007/s10712-019-09525-z)
 744 [z](https://doi.org/10.1007/s10712-019-09525-z), 2019.

745 Guo, L., Wang, Z. B., Townend, I., and He, Q.: Quantification of Tidal Asymmetry and Its Nonstationary
746 Variations, *Journal of Geophysical Research: Oceans*, 124, 773–787,
747 <https://doi.org/10.1029/2018JC014372>, 2019.

748 Haigh, I., Nicholls, R., and Wells, N.: Assessing changes in extreme sea levels: Application to the English
749 Channel, 1900–2006, *Continental Shelf Research*, 30, 1042–1055,
750 <https://doi.org/10.1016/j.csr.2010.02.002>, 2010.

751 Haigh, I. D., Pickering, M. D., Green, J. A. M., Arbic, B. K., Arns, A., Dangendorf, S., Hill, D. F.,
752 Horsburgh, K., Howard, T., Idier, D., Jay, D. A., Jänicke, L., Lee, S. B., Müller, M.,
753 Schindelegger, M., Talke, S. A., Wilmes, S.-B., and Woodworth, P. L.: The Tides They Are A-
754 Changin’: A Comprehensive Review of Past and Future Nonastronomical Changes in Tides, Their
755 Driving Mechanisms, and Future Implications, *Reviews of Geophysics*, 58, e2018RG000 636,
756 <https://doi.org/10.1029/2018RG000636>, e2018RG000636 2018RG000636, 2020.

757 Hersbach, H., Bell, B., Berrisford, P., Biavati, G., Horányi, A., Muñoz Sabater, J., Nicolas, J., Peubey,
758 C., Radu, R., Rozum, I., Schepers, D., Simmons, A., Soci, C., Dee, D., and Thépaut, J.-N.: ERA5
759 hourly data on single levels from 1940 to present, Copernicus Climate Change Service (C3S)
760 Climate Data Store (CDS), <https://doi.org/10.24381/cds.adbb2d47>, 2018.

761 Hinkel, J., Lincke, D., Vafeidis, A. T., Perrette, M., Nicholls, R. J., Tol, R. S. J., Marzeion, B., Fettweis,
762 X., Ionescu, C., and Levermann, A.: Coastal flood damage and adaptation costs under 21st century
763 sea-level rise, *Proceedings of the National Academy of Sciences*, 111, 3292–3297,
764 <https://doi.org/10.1073/pnas.1222469111>, 2014.

765 Horsburgh, K. J. and Wilson, C.: Tide-surge interaction and its role in the distribution of surge residuals
766 in the North Sea, *Journal of Geophysical Research: Oceans*, 112,
767 <https://doi.org/10.1029/2006JC004033>, 2007.

768 Idier, D., Dumas, F., and Muller, H.: Tide-surge interaction in the English Channel, *Natural Hazards and*
769 *Earth System Sciences*, 12, 3709–3718, <https://doi.org/10.5194/nhess-12-3709-2012>, 2012.

770 Idier, D., Bertin, X., Thompson, P., and Pickering, M. D.: Interactions Between Mean Sea Level, Tide,
771 Surge, Waves and Flooding: Mechanisms and Contributions to Sea Level Variations at the Coast,
772 *Surveys in Geophysics*, 40, 1603–1630, <https://doi.org/10.1007/s10712-019-09549-5>, 2019.

773 Ismail, I., Abdullah, W., M Muslim, A., and Zakaria, R.: PHYSICAL IMPACT OF SEA LEVEL RISE
 774 TO THE COASTAL ZONE ALONG THE EAST COAST OF PENINSULAR MALAYSIA,
 775 Malaysian Journal Geosciences, 2, 33–38, <https://doi.org/10.26480/mjg.02.2018.33.38>, 2018.

776 Karri, R. R., Wang, X., and Gerritsen, H.: Ensemble based prediction of water levels and residual currents
 777 in Singapore regional waters for operational forecasting, Environmental Modelling Software, 54,
 778 24–38, <https://doi.org/10.1016/j.envsoft.2013.12.006>, 2014.

779 Keers, J. F.: An empirical investigation of interaction between storm surge and astronomical tide on the
 780 east coast of Great Britain, Deutsche Hydrografische Zeitschrift, 21, 118–125,
 781 <https://doi.org/10.1007/BF02235726>, 1968.

782 Kurniawan, A., Ooi, S. K., and Babovic, V.: Improved sea level anomaly prediction through combination
 783 of data relationship analysis and genetic programming in Singapore Regional Waters, Computers
 784 Geosciences, 72, 94–104, <https://doi.org/10.1016/j.cageo.2014.07.007>, 2014.

785 Kurniawan, A., Tay, S. H. X., Ooi, S. K., Babovic, V., and Gerritsen, H.: Analyzing the physics of non-
 786 tidal barotropic sea level anomaly events using multi-scale numerical modelling in Singapore
 787 regional waters, Journal of Hydro-environment Research, 9, 404–419,
 788 <https://doi.org/10.1016/j.jher.2014.10.005>, 2015.

789 Luu, Q.-H., Tkalic, P., Choo, H. K., Wang, J., and Thompson, B.: A storm surge forecasting system for
 790 the Singapore Strait, Smart Water, 1, 2, <https://doi.org/10.1186/s40713-016-0003-5>, 2016.

791 Marcos, M. and Woodworth, P. L.: Spatiotemporal changes in extreme sea levels along the coasts of the
 792 North Atlantic and the Gulf of Mexico, Journal of Geophysical Research: Oceans, 122, 7031–
 793 7048, <https://doi.org/10.1002/2017JC013065>, 2017.

794 Marzin, C., Rahmat, R., Bernie, D., Bricheno, L., Buonomo, E., Calvert, D., Cannaby, H., Chan, S.,
 795 Chattopadhyay, M., Cheong, W., et al.: Singapore’s second national climate change study–phase
 796 1, chap. 9, E. Met Office, Uk, Centre for Climate Research Singapore, S., National Oceanography
 797 Centre, L., UK, Csiro, A. & Newcastle University, N., UK (ed), 2015.

798 Meteorological Service Singapore: Weather Systems,
 799 http://www.weather.gov.sg/learn_weather_systems, accessed: 2024-05-28.

800 Mohd Anuar, N., Hashim, A. M., Awang, N. A., and Abd Hamid, M. R.: Historical Storm Surges:
 801 Consequences on Coastal Resources and Shoreline Protection in East Coast of Peninsular
 802 Malaysia, pp. 15–18, <https://doi.org/10.15142/T33H1T>, 2018.

803 Mohd Anuar, N., Shafiai, S. H., and Hashim, A. M.: Climate change impact on tropical cyclone evolution
 804 and storm surge severity in the east coast of Peninsular Malaysia, IOP Conference Series:
 805 Materials Science and Engineering, 736, 072 016, [https://doi.org/10.1088/1757-](https://doi.org/10.1088/1757-899X/736/7/072016)
 806 899X/736/7/072016, 2020.

807 Mohd Anuar, N., Teh, H.-M., and Ma, Z.: A Numerical Study on Storm Surge Dynamics Caused by
 808 Tropical Depression 29W in the Pahang Region, Journal of Marine Science and Engineering, 11,
 809 <https://doi.org/10.3390/jmse11122223>, 2023.

810 Ng, P. and Sivasothi, N.: A Guide to the Mangroves of Singapore, Singapore Science centre.,
 811 <https://books.google.com.sg/books?id=7dN9oAEACAAJ>.

812 NOAA: Tide and Current Glossary, <https://tidesandcurrents.noaa.gov/publications/glossary2.pdf>, 2000.

813 Olbert, A. I., Nash, S., Cunnane, C., and Hartnett, M.: Tide–surge interactions and their effects on total
 814 sea levels in Irish coastal waters, Ocean Dynamics, 63, 599–614, [https://doi.org/10.1007/s10236-](https://doi.org/10.1007/s10236-013-0618-0)
 815 013-0618-0, 2013.

816 OpenStreetMap contributors: Planet dump retrieved from <https://planet.osm.org>,
 817 <https://www.openstreetmap.org>, accessed: 2024-07-08, 2017.

818 Prandle, D. and Wolf, J.: Surge-Tide Interaction in the Southern North Sea, in: Hydrodynamics of
 819 Estuaries and Fjords, edited by Nihoul, J. C., vol. 23 of Elsevier Oceanography Series, pp. 161–
 820 185, Elsevier, [https://doi.org/10.1016/S0422-9894\(08\)71277-7](https://doi.org/10.1016/S0422-9894(08)71277-7), 1978.

821 Proudman, J.: The propagation of tide and surge in an estuary, Proceedings of the Royal Society of
 822 London. Series A. Mathematical and Physical Sciences, 231, 8–24,
 823 <https://doi.org/10.1098/rspa.1955.0153>, 1955.

824 Proudman, J.: Oscillations of tide and surge in an estuary of finite length, Journal of Fluid Mechanics, 2,
 825 371–382, <https://doi.org/10.1017/S002211205700018X>, 1957.

826 Pugh, D. T. and Vassie, J. M.: EXTREME SEA LEVELS FROM TIDE AND SURGE PROBABILITY,
 827 Coastal Engineering Proceedings, pp. 52–52, <https://doi.org/10.9753/icce.v16.52>, 1978.

828 Pugh, D. T. and Woodworth, P.: Sea-Level Science: Understanding Tides, Surges, Tsunamis and Mean
829 Sea-Level Changes, chap. 1, p. 1–16, Cambridge University Press,
830 <https://doi.org/10.1017/CBO9781139235778.004>, 2014a.

831 Pugh, D. T. and Woodworth, P.: Sea-Level Science: Understanding Tides, Surges, Tsunamis and Mean
832 Sea-Level Changes, chap. 4, p. 60–96, Cambridge University Press,
833 <https://doi.org/10.1017/CBO9781139235778.007>, 2014b.

834 Pugh, D. T. and Woodworth, P.: Sea-Level Science: Understanding Tides, Surges, Tsunamis and Mean
835 Sea-Level Changes, chap. 7, p. 155–188, Cambridge University Press,
836 <https://doi.org/10.1017/CBO9781139235778.010>, 2014c.

837 Rasmussen, D. J., Bittermann, K., Buchanan, M. K., Kulp, S., Strauss, B. H., Kopp, R. E., and
838 Oppenheimer, M.: Extreme sea level implications of 1.5 °C, 2.0 °C, and 2.5 °C temperature
839 stabilization targets in the 21st and 22nd centuries, *Environmental Research Letters*, 13, 034 040,
840 <https://doi.org/10.1088/1748-9326/aaac87>, 2018.

841 Rossiter, J. R.: Interaction Between Tide and Surge in the Thames, *Geophysical Journal International*, 6,
842 29–53, <https://doi.org/10.1111/j.1-246X.1961.tb02960.x>, 1961.

843 Stephens, S. A., Bell, R. G., and Haigh, I. D.: Spatial and temporal analysis of extreme storm-tide and
844 skew-surge events around the coastline of New Zealand, *Natural Hazards and Earth System*
845 *Sciences*, 20, 783–796, <https://doi.org/10.5194/nhess-20-783-2020>, 2020.

846 Tawn, J. and Vassie, J.: Extreme sea levels: the joint probabilities method revisited and revised,
847 *Proceedings of the Institution of Civil Engineers (London). Part 1 - Design & Construction*, 87,
848 429–442, 1989.

849 Tawn, J. A.: Estimating Probabilities of Extreme Sea-Levels, *Journal of the Royal Statistical Society.*
850 *Series C (Applied Statistics)*, 41, 77–93, <http://www.jstor.org/stable/2347619>, 1992.

851 Tay, S. H. X., Kurniawan, A., Ooi, S. K., and Babovic, V.: Sea level anomalies in straits of Malacca and
852 Singapore, *Applied Ocean Research*, 58, 104–117, <https://doi.org/10.1016/j.apor.2016.04.003>,
853 2016.

854 Tkalic, P., Vethamony, P., Babu, M. T., and Pokratath, P.: Seasonal sea level variability and anomalies
855 in the Singapore Strait, <https://api.semanticscholar.org/CorpusID:67801465>, 2009.

856 Tkalich, P., Vethamony, P., Babu, M. T., and Malanotte-Rizzoli, P.: Storm surges in the Singapore Strait
857 due to winds in the South China Sea, *Natural Hazards*, 66, 1345–1362,
858 <https://doi.org/10.1007/s11069-012-0211-8>, 2013a.

859 Tkalich, P., Vethamony, P., Luu, Q.-H., and Babu, M. T.: Sea level trend and variability in the Singapore
860 Strait, *Ocean Science*, 9, 293–300, <https://doi.org/10.5194/os-9-293-2013>, 2013b.

861 van Maren, D. S. and Gerritsen, H.: Residual flow and tidal asymmetry in the Singapore Strait, with
862 implications for resuspension and residual transport of sediment, *Journal of Geophysical*
863 *Research: Oceans*, 117, <https://doi.org/10.1029/2011JC007615>, 2012.

864 von Storch, H., Jiang, W., and Furmanczyk, K. K.: Chapter 7 - Storm Surge Case Studies, in: *Coastal and*
865 *Marine Hazards, Risks, and Disasters*, edited by Shroder, J. F., Ellis, J. T., and Sherman, D. J.,
866 *Hazards and Disasters Series*, pp. 181–196, Elsevier, Boston, [https://doi.org/10.1016/B978-0-12-](https://doi.org/10.1016/B978-0-12-396483-0.00007-8)
867 [396483-0.00007-8](https://doi.org/10.1016/B978-0-12-396483-0.00007-8), 2015.

868 Williams, J., Horsburgh, K. J., Williams, J. A., and Proctor, R. N. F.: Tide and skew surge independence:
869 New insights for flood risk, *Geophysical Research Letters*, 43, 6410–6417,
870 <https://doi.org/10.1002/2016GL069522>, 2016.

871 Wolf, J.: Interaction of tide and surge in a semi-infinite uniform channel, with application to surge
872 propagation down the east coast of Britain, *Applied Mathematical Modelling*, 2, 245–253,
873 [https://doi.org/10.1016/0307-904X\(78\)90017-3](https://doi.org/10.1016/0307-904X(78)90017-3), 1978.

874 Wolf, J.: Surge-tide interaction in the North Sea and River Thames, *Floods Due to High Winds and Tides*,
875 pp. 75–94, 1981.

876 Woodworth, P. L. and Blackman, D. L.: Evidence for Systematic Changes in Extreme High Waters since
877 the Mid-1970s, *Journal of Climate*, 17, 1190–1197, [https://doi.org/10.1175/1520-](https://doi.org/10.1175/1520-0442(2004)017<1190:EFSCIE>2.0.CO;2)
878 [0442\(2004\)017<1190:EFSCIE>2.0.CO;2](https://doi.org/10.1175/1520-0442(2004)017<1190:EFSCIE>2.0.CO;2), 2004.

879 Wróbel-Niedźwiecka, I., Drozdowska, V., and Piskozub, J.: Effect of drag coefficient formula choice on
880 wind stress climatology in the North Atlantic and the European Arctic, *Oceanologia*, 61, 291–299,
881 <https://doi.org/10.1016/j.oceano.2019.02.002>, 2019.

882 Zhang, X., Chu, D., and Zhang, J.: Effects of nonlinear terms and topography in a storm surge model
883 along the southeastern coast of China: a case study of Typhoon Chan-hom, *Natural Hazards*, 107,
884 551–574, <https://doi.org/10.1007/s11069-021-04595-y>, 2021.

885 Zweers, N. C., Makin, V. K., de Vries, J. W., and Burgers, G.: On the influence of changes in the drag
886 relation on surface wind speeds and storm surge forecasts, *Natural Hazards*, 62, 207–219,
887 <https://doi.org/10.1007/s11069-011-9989-z>, 2012.